J Mater Sci (2011) 46:2947–2954
DOI 10.1007/s10853-010-5170-4

Three-dimensional printing of flash-setting calcium aluminate cement

Anne-Kathrin Maier · Laura Dezmirean · Julia Will · Peter Greil

Received: 4 August 2010 / Accepted: 7 December 2010 / Published online: 22 December 2010

Abstract Three-dimensional indirect printing of flash-setting calcium aluminate cement (CAC) was investigated. Upon water injection into a biphasic mixture of tricalcium aluminate ($3CaO{\cdot}Al_2O_3$) and dodecacalcium heptaaluminate ($12CaO{\cdot}7Al_2O_3$) (phase ratio 0.56/0.44) initially a gel formed acting as a bonding phase which stabilizes the printed object geometry. Post-exposure in water finally resulted in the formation of $2CaO{\cdot}Al_2O_3{\cdot}8H_2O$ and $4CaO{\cdot}Al_2O_3{\cdot}19H_2O$ reaction phases as confirmed by SEM, X-ray diffraction, and FTIR analyses. Reduction of porosity by volume expansion upon hydrolysis reaction from 50% after printing to 20% after post-treatment gave rise for an increase of compressive strength from 5 to 20 MPa, respectively. A bone regenerating scaffold for a micro-vascular loop model was fabricated by 3D printing and hydraulic reaction bonding to demonstrate the potential of using flash-setting calcium aluminate cement powder for biomedical ceramic applications.

Introduction

Three-dimensional printing (3DP) is an additive manufacturing technology used in ceramic prototype manufacturing [1–3]. Typically, 3D printing of ceramic powder systems involves a local solidification reaction of a binder with the injected printing solution. Post-processing of the porous printed parts requires removal of the binder and a subsequent sintering process at high temperatures to consolidate the printed object. Anisotropic packing structure of the bonded powder granules in the printed component may cause a non-uniform densification. Furthermore, a high linear shrinking of typically 15–25% may give rise for reduced dimensional accuracy upon conversion of the printed object into the sintered object.

The flexibility of shaping, however, makes 3DP interesting for the formation of biomedical implants from synthetic materials that are individually tailored to the tissue defect [4]. Thus, for example, biocompatible bone substitutes were manufactured by 3D printing from a variety of materials including tetracalciumphosphate, tricalciumphosphate, hydroxyapatite, etc. [5–7]. In order to reduce high sintering temperatures for consolidation of printed shapes reaction bonding at ambient temperature was applied. For example, tricalcium phosphate (TCP) powder was reaction bonded applying diluted phosphoric acid as printing solution, which triggered local formation of dicalcium phosphate dihydrate under acidic conditions [8, 9].

Hydraulic cement systems may undergo hydrolysis setting reactions and can serve as a bonding system for stabilizing printed shapes during 3DP. A pronounced volume increase upon hydrolysis reaction offers a high potential for reducing the porosity and hence improving the mechanical properties [10]. Calcium aluminate cements (CACs; standard cement chemistry nomenclature: C = CaO, A = Al_2O_3, H = H_2O) are hydraulic setting systems which are widely used for chemical and abrasion resistant devices, high temperature refractories (alumina-rich CACs), and for dental applications [11]. Furthermore, CACs were found to be host cements to produce macro defect-free (MDF) cements [12]. The MDF cement consists of the cement phase, a polymer phase, and an interphase which is formed through the reactions of the polymers and the hydration products. MDF cements have received large attention since

A.-K. Maier (✉) · L. Dezmirean · J. Will · P. Greil
Department of Materials Science (Glass and Ceramics), University of Erlangen-Nürnberg, Martensstr. 5, 91058 Erlangen, Germany
e-mail: Anne-Kathrin.Maier@ww.uni-erlangen.de

early 1980s due to the excellent mechanical properties compared to ordinary cements [10].

In the binary system $CaO–Al_2O_3$ five calcium aluminate compounds C_3A, $C_{12}A_7$, CA, CA_2, and CA_6 exist. As a rule of thumb, the reactivity of calcium aluminates increases as CaO content increases, making C_3A the most reactive compound of these compounds. Thus, tricalcium aluminate cement (C_3A) and dodecacalcium-heptaaluminate cement ($C_{12}A_7$) were found to undergo an accelerated hydrolysis reaction (so-called flash set) with very short reaction times of seconds. The setting kinetics may be varied by addition of accelerators such as Li_2CO_3 or retarders such as citric acid [13]. In 3DP, an aqueous binder solution is injected from a printing head into the powder bed containing the cement phases. Since a typical time period for printing one layer of 50 mm × 50 mm may achieve 10 s biphasic mixtures of $C_3A + C_{12}A_7$ offer a high potential to serve as a reaction bonding system able to stabilize the printed shape within reasonable processing time. Since no high temperature treatment will be necessary for consolidation shrinkage associated with sintering will be avoided and components of complex shape can be processed with excellent dimensional accuracy. Furthermore, $C_3A/C_{12}A_7$ cements were reported to offer a high potential for bone regeneration applications [14]. For example, bioactive CAC was investigated for vertebral body augmentation [15]. Bioactive cements for vertebral augmentation may offer the advantage of providing better integration between the material and the bone, lower curing temperatures and no toxicological effects. The bioactivity, biocompatibility, and resorbability of CA cement can be increased significantly by adding C_3A and $C_{12}A_7$ [14, 16]. In this study, the phase formation reactions of biphasic $C_3A/C_{12}A_7$ cement compositions in the 3D printing process were investigated. The potential for biomedical scaffold manufacturing is demonstrated by forming a 3D bone regeneration scaffold of complex geometrical design.

Experimental procedure

Powder processing

Biphasic mixtures of C_3A and $C_{12}A_7$ with a mass fraction of 1:4 (molar fraction 0.56 C_3A and 0.44 $C_{12}A_7$) (LDSF-LT, Kerneos, Oberhausen, Germany, particle size 1–15 mm) were dry milled down to 25 μm in a planetary ball mill (PM 400, Retsch GmbH, Haan, Germany) with stainless steel balls. The average particle size was measured in the dry mode by laser-granulometric analysis (Master Sizer 2000, Hydro2000S, Malvern Instruments, Malvern, GB). The applied CAC cement is composed of 47.0 wt% Al_2O_3, 50.5 wt% CaO and minor amounts of 0.7 wt% SiO_2, 0.4 wt% MgO, 0.5 wt% Fe_2O_3, and 0.15 wt% TiO_2. The granulated powder formed the powder bed for indirect 3D printing (Z-printer 310, Z Corporation, Burlington, MA). A water–glycerol (15 wt%) binder solution was injected through a bubble jet print head (HP 10 black, Hewlett Packard Inkjet Supplies, Amstelveen, NL) on each individual powder layer (nozzle diameter 60 μm, resolution 450 × 300 dpi). The printing head velocity was set to 0.006 m/s, the resolution was 200 μm. The thickness of a single powder bed layer was set to 100 μm and a liquid/powder weight ratio of 1:3 was applied. The printed objects (specimens as well as demonstrator) were designed using a CAD-program (Solid Edge v.15/academic, PLM Solutions, Huntsville/AL, USA). After drying within the powder bed for 1 h at room temperature, the printed parts were removed and cleaned from the unbound powder by compressed air. Rectangular samples with dimensions of (10 × 10 × 30) mm^3 were printed for compressive strength measurements. One set of samples was 3D printed without any post-treatment (C0 h); another set of samples was additionally soaked in H_2O at room temperature for 24 h (C24 h) and 72 h (C72 h). Furthermore, a modular scaffold developed for a microsurgical arteria/vein loop model was printed as a demonstration part. The scaffold was designed to provide a high potential for stimulation of neovascularisation during bone regeneration [17]. The scaffold is composed of two separate parts which after shape fitting form a scaffold with a circular pore channel (pore channel diameter 2–3 mm) to host the arterio/vein loop and an open porosity in the printed material (average pore size 19 μm) to allow adherence of osteoblast cells. The total size of the scaffolds was 23 mm in diameter and 12 mm in height.

Characterization

Fracture cross sections as well as polished cross sections of the printed and soaked specimens were sputtered with gold for SEM analyses (Quanta 200 instrument, FEI, Prague, Czech Republic). Phase composition was analyzed by means of X-ray powder diffraction (XRD, Kristalloflex, Siemens D 500, Bruker AXS, Karlsruhe, Germany) using monochromatic CuKα radiation ($\lambda = 0.154$ nm). Operating at 30 kV and 30 mA a scan step of 1 s with a step size of 0.02°/2υ over a 2υ range of 5–70° was applied. Phases were identified using ICDD catalog numbers (C_3A: 38-1429; $C_{12}A_7$: 09-0413; C_4AH_{19}: 14-0631, C_2AH_8: 45-0564). Crushed samples were mixed with KBr and pressed for Fourier Transform Infrared Spectroscopy (FTIR, Impact 420 Nicolet Instruments, Madison, USA). The spectra were recorded at frequencies of 4000 to 700 cm^{-1} with a spectral resolution of 2 cm^{-1}. Compressive strength was measured using a universal testing device (Instron 4204, Instron Corp.,

Canton/MA, USA) at a crosshead strain rate of 1 mm/min. The samples were placed between two buffer elastomer layers of 1 mm to ensure uniformity of surface load transfer. Compressive strength was averaged from the failure stresses of 20 samples. For the determination of the pore size distribution, a high-pressure mercury intrusion porosimeter (Pascal 140, Thermo Electron, Rodano/Milan, Italy) was used. Pores of diameters ranging from 0.1 to 100 μm were detected. The samples were cylinders of 10 mm diameter and 10 mm length.

Results and discussion

Hydraulic setting reaction

Hydration of CAC proceeds through dissolution of CAC and subsequent precipitation of calcium aluminate hydrates, which is accompanied by decrease of porosity and increase of strength [13, 18]. After injection of water through the print head into the powder bed the calcium aluminate phases start to dissolve in water as calcium ions Ca^{2+} and aluminum hydroxide $[Al(OH)_4]^-$. This continues until the saturation level is reached. The pH of the liquid phase rises up ($\sim$12). Nucleation and precipitation of calcium aluminate hydrate crystals occur together with alumina hydroxide gel (AH_x) or crystalline Gibbsite (AH_3)

$$2C_3A + 27H \rightarrow C_4AH_{19} + C_2AH_8 \quad (1)$$

$$C_{12}A_7 + 51H \rightarrow 6C_2AH_8 + AH_3 \quad (2)$$

Dissolving, nucleation, and precipitation are an ongoing process as long as enough water is available for dissolution of the CAC phases. C_2AH_8 and C_4AH_{19} are meta-stable and will eventually convert to the hydrogarnet phase C_3AH_6 at elevated temperatures which is associated with a pronounced increase of porosity because the density of C_3AH_6 is higher than that of C_2AH_8. Addition of fumed silica, for example, was demonstrated to avoid reformation and stabilize the primary hydrolysis products [19]. In 3D printing process, however, the amount of injected water is limited and the process is interrupted at an intermediate state providing sufficient strength for specimen handling and purification. Subsequently, the specimen is immersed in water for various periods to complete the reactions shown above.

Figure 1 shows the microstructure of the printed multilayer of samples without post-processing (C0 h) and after soaking in water for 24 h (C24 h) and 72 h (C72 h), respectively. No delamination was observed at the interfaces between the individual layers. In the area where the water was injected hydrolysis reaction took place with the injected water acting as a weak acid on the basic cement powder. Initially, dissolution of C_3A and $C_{12}A_7$ triggers the formation of a $Al(OH)_3$-gel that acts as a bonding phase between undissolved particles [20, 21]. After soaking in water for 24 h, formation of crystalline C_2AH_8 and C_4AH_{19} was detected by XRD. After 72 h a widespread network of intermingling crystals has developed which fill up the pore space and reduce total porosity. The calcium–alumohydrate phases form crystals of platelet morphology, which are hexagonal or pseudohexagonal, with (0001) cleavage and may give rise for interlocking between the crystals.

Figure 2 shows the XRD pattern of printed samples. The peaks of 3D printed C0 h samples matched the spectra of C_3A and $C_{12}A_7$. No other crystalline hydration products were observed immediately after the initial bonding reaction during the printing process. After immersion for 24 h (C24 h) XRD revealed the presence of hydrolysis reaction products C_2AH_8 and C_4AH_{19} as to be expected from Eqs. 1 and 2. The XRD patterns recorded from C72 h samples show almost complete conversion of C_3A to C_2AH_8 and C_4AH_{19} whereas the amount of $C_{12}A_7$ is reduced but still present.

Figure 3 shows the FTIR absorption spectra. 3D printed samples without post-processing show a broad peak at 750–900 cm^{-1}, which corresponds to the asymmetric stretching vibration of Al–O bonds of $[AlO_4]$-tetrahedra in C_3A and $C_{12}A_7$ [22, 23]. With increasing time of hydrolysis reaction this peak diminishes whereas OH stretching modes of $Al(OH)_3$ appear at 3380–3400 cm^{-1} [24]. Furthermore, typical absorption bands at 3600–3700 cm^{-1} become visible, associated to $C_3A/C_{12}A_7$ hydration products [23]. Additive bands at 3473, 3531, and 1022 cm^{-1} are ascribed to OH stretching vibration in hydrates of calcium aluminate cements [24, 25]. The bands at 1646 and 1380 cm^{-1} can be ascribed to bending vibrations of adsorbed water [24, 26]. The intensity of the bands associated to hydration reaction increases and confirms the XRD and SEM analyses. The results of SEM, XRD, and IR analyses give indication that hydrolysis initially triggers the formation of an amorphous hydroxide gel followed by the crystallization of hydroxide phases with prolonged exposure to water.

The main factor influencing the strength properties of the obtained samples was found to be their porosity. Mercury intrusion porosimetry was used to analyze the pore size distribution in the printed specimens, Fig. 4. The pore system in cement-based materials consists of four types of pores. These are: (a) gel pores, which are pores of characteristic dimension <0.01 μm; (b) capillary pores with average radius ranging from 0.005 to 5 μm; (c) macropores due to deliberately entrained air; and (d) macropores due to inadequate compaction [27]. As Fig. 4 shows, the printed sample exhibits a monomodular pore size distribution with a major peak of macropores extending from approximately 10 to 60 μm. After 24 h immersion

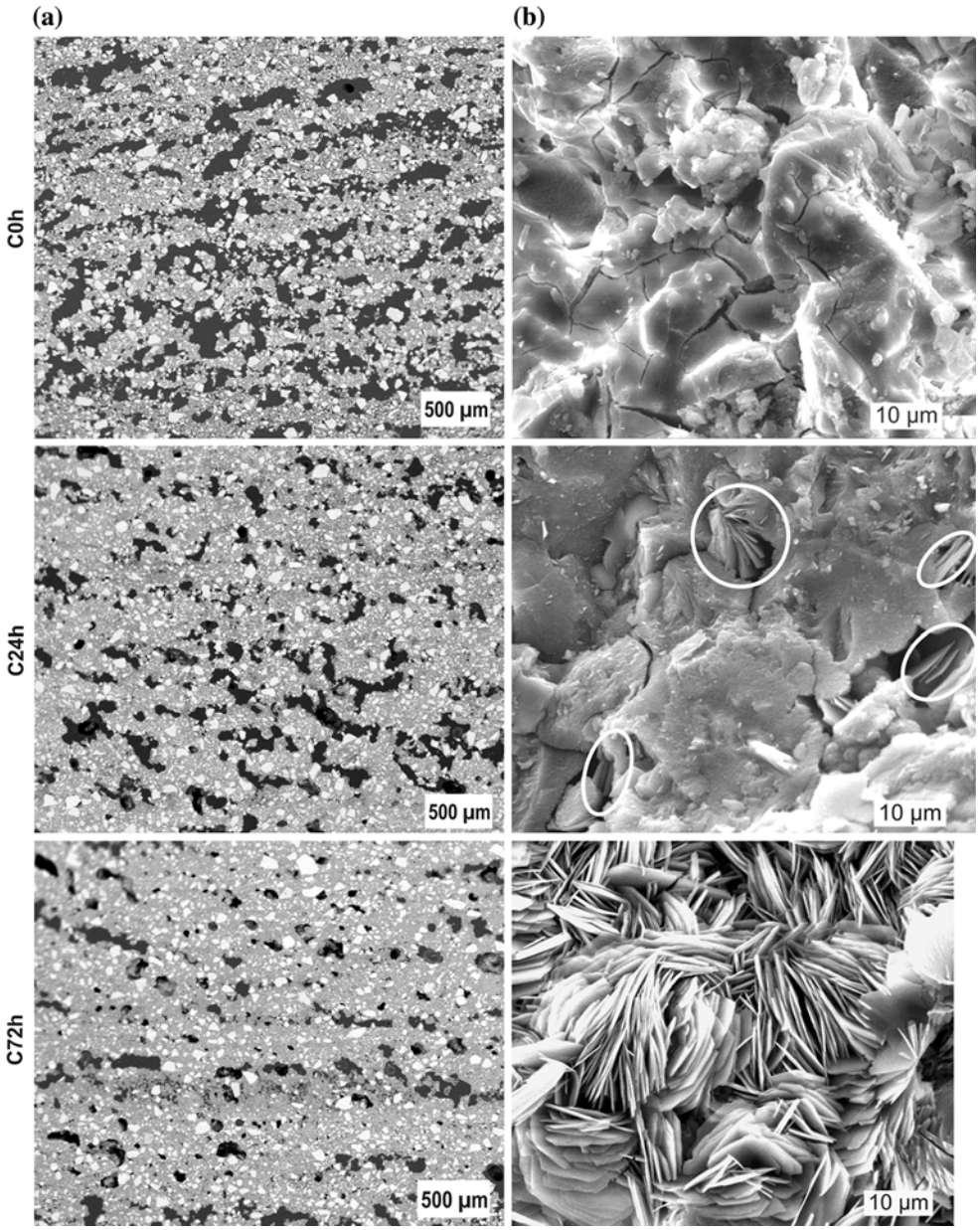

Fig. 1 Microstructure (SEM) of 3D printed CAC samples soaked in water for various periods (polished cross sections)

in water the macropore peak reduced significantly in intensity and a broad peak of capillary pores extending from <0.1 to 3 µm was observed. Further hydrolysis reaction for 72 h finally resulted in the closure of pores larger than approximately 3–5 µm and a peak with a maximum at approximately 0.4–0.5 µm dominates. Since the gel pores, which are below 0.01 µm do not influence the strength of the hydrolysis reaction product adversely through its porosity those pores sizes were not measured, although these pores are directly related to creep and shrinkage [28]. Capillary pores and other larger pores, on the other hand, are responsible for reduction in strength and elasticity [29].

The crystallization of the calcium aluminate hydrate phases is associated with a volume change, which for stoichiometric hydrolysis reaction (Eqs. 1, 2) can be expressed by the molar volumes of species i, V_i, (Table 1):

$$\frac{\Delta V}{2V_{C_3A}} = \frac{V_{C_4AH_{19}} + V_{C_2AH_8} - 2V_{C_3A}}{2V_{C_3A}} = 2.1 \quad (3)$$

$$\frac{\Delta V}{V_{C_{12}A_7}} = \frac{6V_{C_2AH_8} + V_{AH_3} - V_{C_{12}A_7}}{V_{C_{12}A_7}} = 1.26 \quad (4)$$

Thus, hydrolysis setting reaction will cause an increase of fractional density and a reduction of residual porosity. The porosity in the hydrolysis reaction product, P_{hr}, may be expressed to a first approximation as a function of the

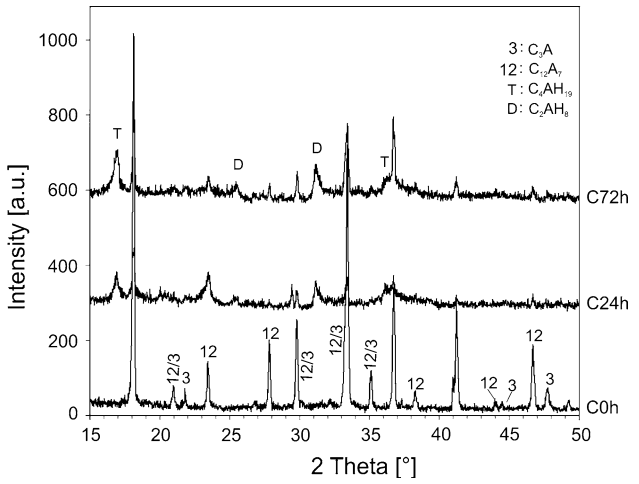

Fig. 2 XRD patterns recorded from samples after various soaking periods in water

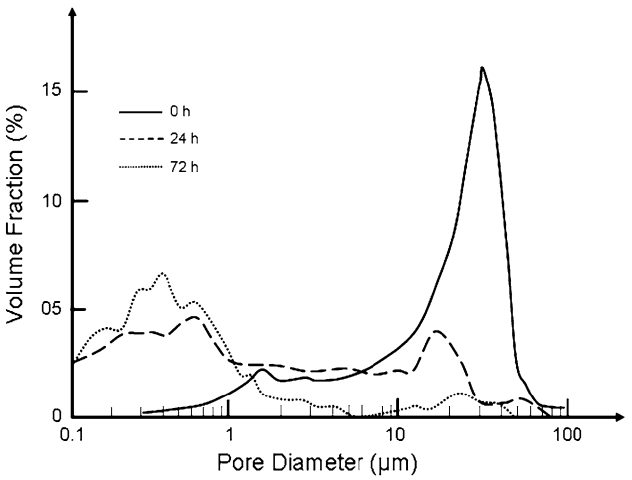

Fig. 4 Pore size distributions of the CAC samples soaked for various periods in water

Fig. 3 FT-IR spectra of samples soaked for various periods in water

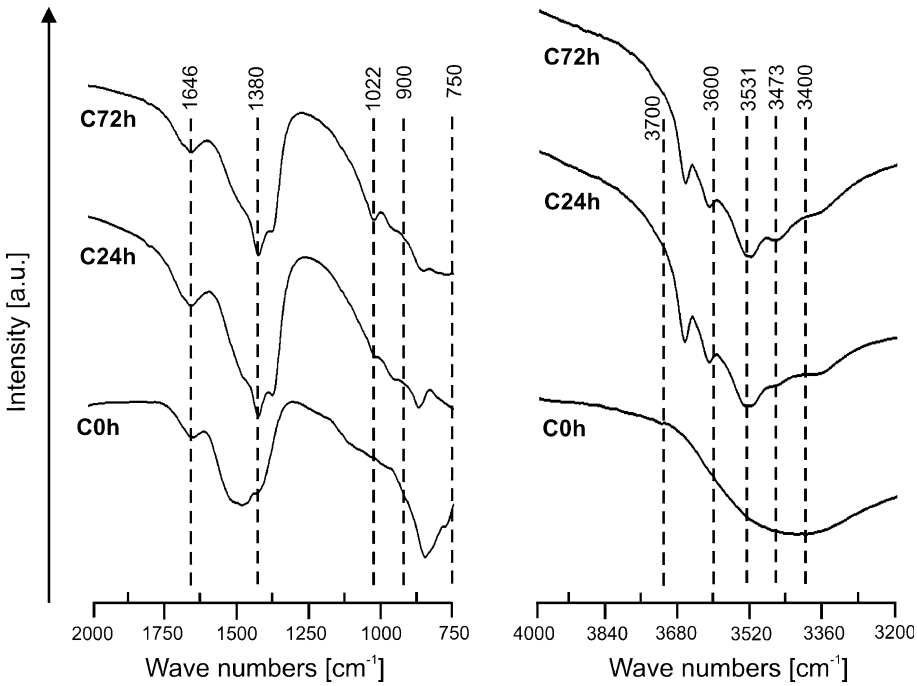

initial fractional green density (e.g., the packing density in the printed body), ρ_{pr}*, and the specific volume changes associated with hydrolysis reaction (expansion) and drying (shrinkage) by

$$P_{hr} = 1 - \rho_{pr} * \left(1 + \sum_i \left[\frac{\Delta V}{V_0}\right]_i\right) \quad (5)$$

For biphasic mixtures of C_3A and $C_{12}A_7$ the volume change is given by the molar fractions x_i with $i = C_3A$ and $C_{12}A_7$, respectively,

$$\left[\frac{\Delta V}{V_0}\right]_{hr} = f \sum x_i \frac{\Delta V_i}{V_i} = f(x_{C_3A} 2.1 + (1 - x_{C_3A}) 1.26) \quad (6)$$

f is a hydrolysis factor which corresponds to the printed cement/water ratio and may vary from $f = 0$, no hydrolysis, to $f = 1$, stoichiometric hydrolysis. In the case the printed and reacted body undergoes shrinkage during drying (i = sh):

$$\left[\frac{\Delta V}{V_0}\right]_{sh} = (1 + \varepsilon_x)(1 + \varepsilon_y)(1 + \varepsilon_z) - 1 \quad (7)$$

Equation 5 is expanded with ε_x, ε_y, and ε_z denoting the linear shrinkages measured in the three principal directions (measured values of $\varepsilon_x = +0.009$, $\varepsilon_y = +0.016$, $\varepsilon_z = -0.02$). Figure 5 shows the reduction of residual porosity in the printed body with ongoing hydrolysis reaction

Table 1 Crystallographic data of CA and CAH phases

Phase	Crystal structure	Density (g/cm^3)	Molar volume (cm^3/mol)	References
C_3A	Cubic (Pa3)	3.04	88.9	[39–41]
$C_{12}A_7$	Cubic ($I\bar{4}3d$)	2.69	551.6	[42]
C_4AH_{19}	Rhomboedric ($R\bar{3}c$, R3c) or hexagonal ($P6_322$, $P6_3/m$, $P6_3$)	1.80	317.5	[41, 43–45]
C_2AH_8	Hexagonal (no space group reported)	1.95	183.7	[40, 46, 47]

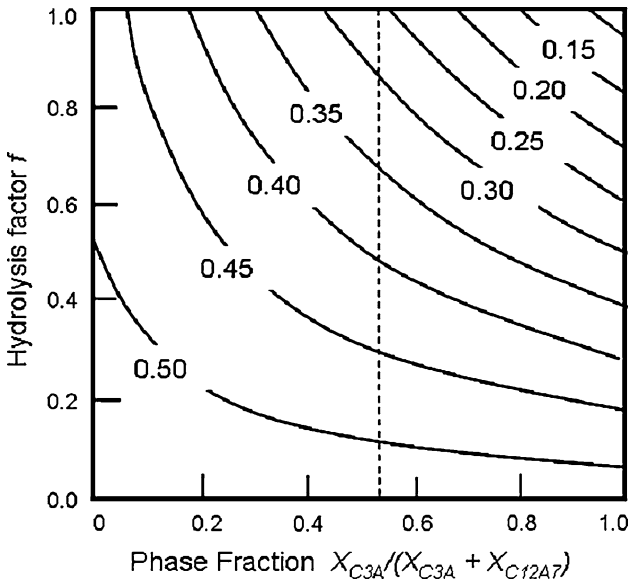

Fig. 5 Porosity in the 3D printed CAC samples calculated from Eq. 5 as a function of CAC composition and degree of hydrolysis. The *dashed line* indicates the sample composition

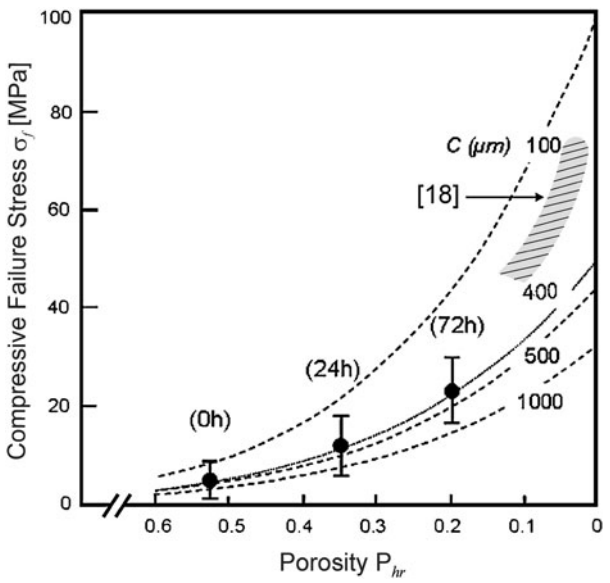

Fig. 6 Compressive strength of printed specimens measured after various soaking (hydrolysis) periods and calculated values assuming various defect sizes c according to Eq. 8. For reference data of CAC with CA as the major phase are shown (hatched region) [18]

proceeds during exposure in water. After 72 h an experimental value of residual porosity of 20% was measured which coincides reasonably well with the value (26%) calculated according to Eq. 5. Further reduction of porosity may be achieved either by increasing the packing density in the printed body by applying powders with multimode particle size distribution or by increasing the molar fraction of C_3A in the starting cement system.

Compressive strength

While rapid hardening behavior of calcium aluminate cements make them candidates for new shaping processes such as 3D printing, those cements were reported to suffer from low strength and toughness [10]. Figure 6 shows the compressive strength of the printed specimens after various immersion periods in water. As the hydration process continues more and more hydrate crystals are developed and grow, interweaving with one another, giving strength to the structure. Initially low compression strength of 5 ± 2 MPa was measured at a porosity of approximately 52% which after 72 h exposure to water raised to 20 ± 5 MPa at a reduced porosity of 20%.

Increase of compressive strength is viewed as a consequence of the hydration process and decrease of porosity and size and density of flaws [29]. Traditionally, it had been believed that cement strength depended mainly on the volume of pores in the material. A variety of relations expressing the strength (flexurals strength, compression strength) with a power law function of the porosity were reported in literature. For example, Matusonovic et al. [18] studied the compressive strength of CACs for porosites ranging form 0.1–0.5. A scaling law of the type $\sigma = \sigma_0(1 - P/P_0)^2$, where σ_0 equals the failure stress at zero porosity and P_0 denotes the porosity at zero strength (e.g., the porosity of the freshly prepared cement paste) were shown to fit the experimental data well. In contrast, it was also thought that cement behaved as a brittle material, in which case the presence of long cracks would be most critical [30]. Taking into account the influence of porosity P as expressed by previous relations such as those of Frankenstein, Feret, and Ryshkewitch, as well as the brittle

failure due to large flaws of size c inherent in the microstructure of the cement [31], a modified relation for the failure stress (flexural strength) was derived [32]:

$$\sigma_f = \left[\frac{E_0\gamma_0}{\pi c}(1-P)^3\exp(-kP)\right]^{1/2} \quad (8)$$

E_0 and γ_0 are the Young's modulus and fracture energy, respectively, of the dense material ($P = 0$) and k is a pore geometry factor (k varies from 1 to 9 and attains approximately 5 for pores of spherical shape). As Fig. 6 shows, the measured data points fit well to the calculated behavior according to Eq. 8 taking reasonable values for $k = 5$, $E_0 \sim 20$ GPa, $\gamma_0 \sim 20$ J/m^2 [32], and $c \sim 400$ μm. Thus, reduction of porosity as well as removal of large defects from the printed cement paste are major targets to improve the loading capacity of 3D printed hydraulic cement systems. Depending on the water to cement ratio compression strength values for CACs ranging from 15 to 35 MPa were measured at a total porosity of 20% which increased to a maximum value of 80 MPa for a low porosity material with $P < 7\%$ [18].

Strong cements can be produced by a variety of technologies—press-molding, extruding, roll-compacting, roll-milling, etc., of cement powder—which have in common that a high packing density and reduced flaw size is achieved by the help of an external applied stress. In contrast, 3D printing commonly suffers from relatively low packing densities of the powder bed (<0.5) which is formed by the mechanical transport process of the powder to the powder bed. Transport and pre-densification supported by chemical (rheology) and physical (vibration) means to achieve a higher packing density containing smaller pores and flaws must be a goal to be addressed in future development of 3D printing process for hydraulic setting systems.

Bone regeneration scaffold demonstrator

Similar to HA cements which are attractive materials for orthopedic applications because they can be molded into shape during implantation and offer the potential of being applied with minimally invasive techniques [33], CACs may offer a high potential for biomedical applications. Measurements of the cytotoxicity of a calcium aluminate cement in comparison with other dental cements and resin-based materials confirmed the potential for use in implant devices [34]. Since setting reaction occurs at ambient temperature loading with biofunctional additives sensitive to thermal degeneration offers a versatile route for functionalization of porous scaffolds. Since hydraulic setting consolidation does not require high temperatures, biofunctional additives, such as protein-based growth factors or antibiotics may be incorporated in the printed scaffolds during the printing process [35–37]. Calorimetric measurements revealed a reduction of heat release from 323 to 205 J/g using a water–glycerol (15 wt%) binder solution instead of pure water during 3D printing. Furthermore, no temperature change could be detected experimentally during post-treatment in water when the gel converts to C_2AH_8 and C_4AH_{19}.

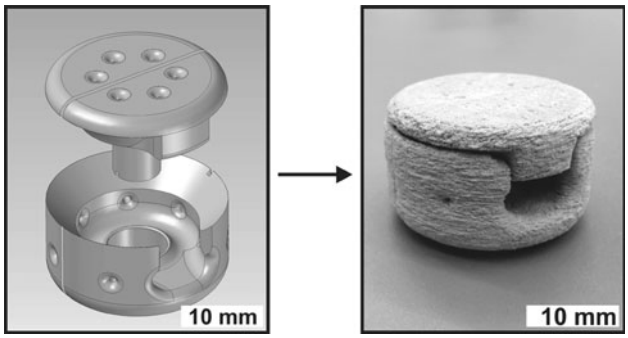

Fig. 7 Bone regeneration scaffold CAD design (*left*) and printed scaffold (*right*) for micro-surgical arterio-vein loop model according to Kumar and Bhattacharjee [38]

Figure 7 shows a bone regeneration scaffold developed for bone reconstructive surgery. The macroscopic design of the modular scaffold offers suitable geometrical conditions for the preparation of an arterio-venous loop prepared to trigger vascularisation as described elsewhere [17, 38]. The arterio-venous loop (AV loop) model is gaining importance as a means of initiating and sustaining perfusion in tissue engineering constructs in vivo. An anisotropic linear dimensional change was observed with *in-plane* directions showing a small expansion with $\varepsilon_x = +0.9\%$ and $\varepsilon_y = +1.6\%$ whereas a small shrinkage was found in the direction perpendicular to the printed planes ($\varepsilon_z = -2\%$).

Conclusions

Calcium aluminate cements offer a high potential of being used in 3D printing of objects consolidated by a rapid hydrolysis reaction. Tailoring the porosity is a key factor to improve the mechanical properties of the printed object. Since the outer dimensions of a printed object only slightly change upon hardening reaction selective volume expansions associated with the hydrolysis of the aluminate cement phases gives rise for a reduction of porosity. With increasing void filling by hydration products, i.e., increasing density of the microstructure and refinement of the pore structure of the matrix, there is also an increase in the compression strength. Thus, flash setting CAC cement systems might offer novel applications for printable ceramics which do not require high temperature sintering for consolidation as demonstrated by 3D printing of a bone regeneration scaffold of complex geometry.

Acknowledgements The financial support from DFG (GR 961/27) is gratefully acknowledged. The authors want to thank Dr. Nahum Travitzky for his technical support in terms of 3D printing. Anne-Kathrin Maier would also like to express her heartfelt thanks to PD Dr. Friedlinde Götz-Neunhoeffer at the Department of Mineralogy, University of Erlangen-Nuremberg, Germany for her helpful comments during the preparation of this manuscript.

References

1. Sachs E, Haggerty JS, Cima MJ, Williams PA (1993) US Patent No. 5204055
2. Cawley JD (1999) Curr Opin Solid State Mater Sci 4:483
3. Tay BY, Evans JRG, Edirisinghe MJ (2003) Int Mater Rev 48:341
4. Leong KF, Cheah CM, Chua CK (2003) Biomaterials 24:2363
5. Leukers B, Gulkan H, Irsen SH, Milz S, Tille C, Schieker M, Seitz H (2005) J Mater Sci Mater Med 16:1121
6. Khalyfa A, Meyer W, Schnabelrauch M, Vogt S, Richter HJ (2006) Ceram Forum Int 83(13):23
7. Deisinger U, Irlinger F, Pelzer R, Ziegler G (2006) Ceram Forum Int 83(13):75
8. Pfister A, Walz U, Laib A, Muhlhaupt R (2005) Macromol Mater Eng 290:99
9. Gbureck U, Hölzel T, Klammert U, Würzler K, Müller FA, Barralet JE (2007) J Control Release 122:173
10. Birchall JD, Howard AJ, Kendall K (1981) Nature 289:388
11. Scrivener KL, Cabiron JL, Letourneux R (1999) Cem Concr Res 29:1215
12. Pushpalal GKD, Kobayashi K, Kawano T, Maeda N (1999) Cem. Concr. Res. 29(1):121
13. Rodger SA, Double DD (1984) Cem Concr Res 14(1):73
14. Oh SH, Finones R, Jin S, Choi SY, Kim KN (2004) J Mater Res 19:1062
15. Hulme PA, Heini PF, Persson T, Spengler H, Björklund K, Hermansson L, Ferguson SJ (2006) Eur Cells Mater 11(1):42
16. Graves GA, Hentrich RL, Stein HG, Bajpal PK (2004) J Biomed Mater Res 5:91
17. Will J, Melcher R, Treul C, Travitzky N, Kneser U, Polykandriotis E, Horch R, Greil P (2008) J Mater Sci Mater Med 19:2781
18. Matusinovic T, Sipusic J, Vrbos N (2003) Cem Concr Res 33:1801
19. Hidalgo A, Petit S, García JL, Alonso C, Andrade C (2007) Stud Surf Sci Catal 170:1617
20. Meredith P, Donald AM, Meller N, Hall C (2004) J Mater Sci 39:997. doi:10.1023/B:JMSC.0000012933.74548.36
21. Black L, Breen C, Yarwood J, Deng CS, Phipps J, Maitland G (2006) J Mater Chem 16:1263
22. Tas AC (1998) J Am Ceram Soc 81:2853
23. Lavat AE, Grasselli MC (2007) AZO J Mater Online 3:1
24. Lee DH, Condrate RA (1995) Mater Lett 23:241
25. Hidalgo A, Garcia JL, Alonso MC, Fernandez L, Andrade C (2009) J Therm Anal Calorim 96:335
26. Radwan MM, Heikal M (2005) Cem Concr Res 35:1601
27. Odler I, Rößler M (1985) Cem Concr Res 15:320, 402
28. Reinhardt RW, Gaber K (1990) Mater Struct 23:3
29. Kumar R, Bhattacharjee B (2003) Cem Concr Res 33:155
30. Kendall K (1987) J Eur Ceram Soc 12:21
31. Takahashi T, Yamamoto M, Ioku K, Goto S (1997) Adv Cem Res 9:25
32. Kendall K, Howard AJ, Birchall JD (1983) Philos Trans R Soc A 310:139
33. Yuan HP, Li YB, de Bruijn JD, de Groot K, Zhang X (2000) Biomaterials 21:1283
34. Franz A, Konradsson K, König F, Van Dijken JWV, Schedle A (2006) Acta Odontol Scand 64:1
35. Gbureck U, Hölzel T, Doillon CJ, Müller FA, Barralet JE (2007) Adv Mater 19:795
36. Habibovic P, Gbureck U, Doillon CJ, Bassett DC, van Blitterswijk CA, Barralet JE (2008) Biomaterials 29(7):944
37. Vorndran E, Klammert U, Ewald A, Barralet JE, Gbureck U (2010) Adv Funct Mater 20(10):1585
38. Polykandriotis E, Tjiawi J, Euler S, Arkudas A, Hess A, Brune K, Greil P, Lametschwandtner A, Horch RE, Kneser U (2008) Microvasc Res 75(1):25
39. Neunhoeffer FG, Neubauer J (1997) Proceedings of the 10th international Congress on the Chemistry of Cement, Goeteborg, vol 10, p 56
40. Taylor HFW (1997) Cement chemistry. Academic Press, London
41. Clifton JR, Ponnersheim JM (1994) NISTIR 5390:1
42. Nishio Y, Nomura K, Miyakawa M, Hayashi K, Yanagi H, Kamiya T, Hirano M, Hosono H (2008) Phys Status Solidi A 205:2047
43. Rashid S, Barnes P, Bensted J, Turrillas X (1994) J Mater Sci Lett 13:1232
44. Aruja E (1961) Acta Cryst 14:1213
45. Roberts MH (1968) ISCC II-29 Tokyo, pp 104
46. Ukrainczyk N, Matusinovic T, Kurajica S, Zimmermann B, Sipusic J (2007) Thermochim Acta 464:7
47. Odler I (2000) Special inorganic cements. Spon Press, London